Journal of Applied Physics

Laser-induced vaporization of a stretching sheet of liquid tin

Cite as: J. Appl. Phys. **129**, 053302 (2021); https://doi.org/10.1063/5.0036352
Submitted: 04 November 2020 . Accepted: 15 January 2021 . Published Online: 02 February 2021

Bo Liu, Randy A. Meijer, Javier Hernandez-Rueda, Dmitry Kurilovich, Zeudi Mazzotta, Stefan Witte, and Oscar O. Versolato

Journal of Applied Physics ARTICLE scitation.org/journal/jap

Laser-induced vaporization of a stretching sheet of liquid tin

Cite as: J. Appl. Phys. **129**, 053302 (2021); doi: 10.1063/5.0036352
Submitted: 4 November 2020 · Accepted: 15 January 2021 ·
Published Online: 2 February 2021

Bo Liu,[1,2] Randy A. Meijer,[1,2] Javier Hernandez-Rueda,[1] Dmitry Kurilovich,[3] Zeudi Mazzotta,[1] Stefan Witte,[1,2] and Oscar O. Versolato[1,2,a)]

AFFILIATIONS

[1]Advanced Research Center for Nanolithography (ARCNL), Science Park 106, 1098 XG Amsterdam, The Netherlands
[2]LaserLab, Department of Physics and Astronomy, Vrije Universiteit Amsterdam, De Boelelaan 1105, 1081 HV Amsterdam, The Netherlands
[3]ASML Netherlands B.V., De Run 6501, 5504 DR Veldhoven, The Netherlands

[a)]**Author to whom correspondence should be addressed:** o.versolato@arcnl.nl

ABSTRACT

We experimentally study the mass distribution of a sheet of liquid tin formed by the impact of a ns-laser pulse on a spherical microdroplet. The mass distribution is obtained using a low-intensity, second ns-laser pulse, which induces vaporization of the stretching thin tin sheet. This careful vaporization enables the investigation of the thickness profile of the sheet, and its mass, at early times after laser pulse impact on a droplet, which have remained inaccessible by the methods used in recent work [B. Liu *et al.*, Phys. Rev. Appl. **13**, 024035 (2020)]. The vaporization method, moreover, allows the visualization of the thick rim that bounds the thin sheet. Our results unambiguously demonstrate that increasing the energy of the ns-laser pulse incident on the droplet, which enables reaching a predetermined target radius more quickly, results in a larger mass fraction remaining in the sheet. Specifically, our studies show a doubling of the sheet mass fraction by reducing the required expansion time. As a corollary, less tin will end up in other channels of the mass distribution, such as fragments surrounding the sheet. Accordingly, more mass would be available in the target sheet for interaction with the more energetic, main laser pulse that is used in the industry to produce a hot and dense plasma from tin sheet targets in order to create extreme ultraviolet light for nanolithography.

I. INTRODUCTION

State-of-the-art nanolithography machines make use of extreme ultraviolet (EUV) light, which enables the continued miniaturization of semiconductor devices.[1–6] In order to generate the EUV radiation, liquid tin microdroplets are used as mass-limited targets in a dual-laser-pulse irradiation sequence. First, a nanosecond laser pulse, termed *pre-pulse* (PP), irradiates the tin microdroplet, causing it to deform into a liquid sheet within a few microseconds.[7–12] The sheet typically has a diameter of several hundreds of micrometers and thickness of several tens of nanometers.[10,11] As the sheet expands, a bounding rim is formed at the edge of the sheet.[11] From this rim, a myriad of small fragments is propelled outwards along the radial direction.[8–12] When the sheet has reached a specified diameter, a second, more energetic *main-pulse* is used to generate a dense and hot tin plasma that emits the relevant EUV radiation.[13]

Recently, our group reported on the hydrodynamic mechanisms that govern the thickness profile of nanosecond laser-induced sheets of liquid tin.[11] The experimental observations were used to benchmark a physical model that predicts the instantaneous sheet thickness and, from that, the mass of the sheet. Building on previous works,[7,14–17] our research further confirmed the continuous loss of mass from the sheet over time. Remarkably, less than half of the initial amount of tin was found to remain in the sheet under currently relevant industrial conditions.[11,18,19] This finding is particularly pertinent in the context of EUV source lifetime, which is adversely impacted by tin debris. Our results further indicated that using a relatively more energetic PP could be beneficial: increasing the PP energy leads to a faster initial expansion rate of the target sheet, and thus any desired sheet size is reached earlier in the expansion trajectory, when more tin is carried by the sheet.

To validate this proposition, knowledge of the sheet morphology at earlier times is needed. Since, inherently, the two methods previously used in Ref. 11 to determine the thickness profile are limited to mid- and late-time delays, we here employ an alternate method that is based on laser-induced vaporization. In this case, the sheets to be investigated will be irradiated by an auxiliary laser pulse, termed *vaporization pulse* (VP). This VP induces vaporization that gradually thins, or rarefies, the sheet into a mist comprising nanoparticles and, possibly, atomic tin. The vaporization process serves as a probe to estimate the amount of tin carried by the sheet: by measuring the time required to locally vaporize the sheet, we can infer its thickness profile at early time delays unattainable by the previously used methods. The obtained sheet thickness profile finally yields the fraction of the initial volume (or, equivalently, mass) still contained in the sheet.

In this paper, we investigate the tin mass distribution during laser-induced droplet deformation by introducing a method that allows us to obtain thickness profiles from careful laser-induced vaporization. Three target sheets are selected, representing the mass distributions formed using various PP energies and at different stages of the expansion process. All these targets share a common sheet radius $R_{\mathrm{sheet}} \approx 210\,\mu\mathrm{m}$ (referred to as $R^{\star}$ hereafter) when we probe their thickness profile and mass content using the auxiliary VP. This common sheet radius $R^{\star}$ lies within the range of diameters relevant for EUV generation in an industrial setting[18,19], where this diameter range is set to a large degree by the diameter of the main-pulse. We use two different PP laser energies to demonstrate a higher mass content to be contained within the sheet when employing a higher PP energy. Additionally, we investigate two targets resulting from a constant PP energy yet at different moments during the expansion trajectory. We discuss the results stressing the importance of the time delay after the PP impact on the droplet as the key parameter that ultimately determines the mass distribution of the target.

II. EXPERIMENT AND METHODS

In the experiment, a droplet generator, mounted on a tiltable bellow assembly, dispenses a vertically aligned microdroplet train of liquid tin (temperature 260 °C, density $\rho = 6968\,\mathrm{kg/m^3}$, and surface tension $\sigma = 0.55\,\mathrm{N/m}$) into a vacuum environment (10^{-7} mbar) with a velocity and repetition rate of approximately $10\,\mathrm{m\,s^{-1}}$ and 31.5 kHz, respectively. The droplets have a diameter of $D_0 = 2R_0 \approx 29\,\mu\mathrm{m}$ (where R_0 is the droplet radius that is established with an uncertainty of $\pm 0.5\,\mu\mathrm{m}$) and a stable position, with instabilities on the order of a single micrometer in both horizontal and vertical directions. The droplet stream passes through a horizontal light sheet produced by a helium–neon laser and positioned approximately 2 mm above the center of the vacuum vessel, i.e., the laser–droplet interaction point. The consequent light scattered by the droplets is detected by a photo-multiplier tube and the kHz-frequency signal is down-converted to 10 Hz to serve as a trigger for the acquisition and laser systems. For further details on the droplet generator setup, see also Ref. 20.

Two circularly polarized laser beams from independent Nd:YAG systems operating at 1064 nm wavelength are collinearly aligned onto the droplet.[21] The timing sequence of the laser pulses from these two systems is illustrated in Fig. 1(a). The PP, with a Gaussian 10 ns (full width at half maximum, FWHM) temporal shape, is focused down to a Gaussian spot with a size of 55 μm (FWHM) at the location of the droplet. The VP, delayed by a time interval Δt, is produced by an in-house built system with arbitrary pulse shaping capabilities.[22] The system is programmed to output a temporally square 50 ns pulse, and its top-hat spatial profile is imaged onto the target with a beam diameter of $\approx 950\,\mu\mathrm{m}$. Therefore, the VP has a constant intensity distribution [denoted as I_{VP} $(\mathrm{W/m^2})$], both spatially and temporally.

The dynamics of the irradiated targets are captured by stroboscopic shadowgraphy imaging systems.[8,11,12] These systems combine incoherent pulsed backlight-illumination at 560 nm with CCD cameras coupled to long-distance microscopes, yielding a spatial resolution of approximately 5 μm. A dye laser provides the backlighting shadowgraphy pulses (SPs) with a spectral bandwidth of 12 nm (FWHM) and a pulse duration of 5 ns (FWHM). As depicted in Fig. 1(a), the shadowgraphy systems simultaneously provide front- and side-view images of the tin targets, with 30° and 90° angles with respect to the Nd:YAG laser beam propagation direction, respectively.

Initial optimization of the PP laser-to-droplet (L2D) alignment is performed by observing the target tilt and center-of-mass velocity U using the shadowgraphy systems.[21] As droplet position and beam pointing instabilities are on the order of single micrometers, no additional active stabilization is needed. Per shadowgraphy time delay, multiple (typically 10) frames are recorded to allow for post-filtering on optimal L2D.

Figure 1(a) (upper right panel) illustrates the typical response of a droplet to the impact of a PP.[7–11] The droplet is rapidly propelled to the velocity U on the order of 100 m/s along the propagation direction of the laser.[8,9] Furthermore, the droplet deforms into an axisymmetric sheet that radially expands to a size R_{sheet} over *time* (indicated as t hereafter, where $t = 0$ marks the arrival of the PP). These orthogonal motions, characterized by U and the initial expansion rate immediately after laser pulse impact $\dot{R}(t = 0)$ (referred to as $\dot{R}_0$ hereafter), are driven by plasma pressure.[8–10] Typically, $\dot{R}_0 \sim U$ as in the analogous case of droplet-pillar impact studied in Ref. 14. The timescale of the acceleration is similar to the laser pulse length (∼ns), vastly shorter than the timescale of the ensuing fluid dynamic deformation (∼μs).[6,7]

The sheet is irradiated by the VP [see Fig. 1(a), lower left panel] when it acquires a radius of $R^{\star}$. This onset moment of the VP is referred to as $t_{\mathrm{VP}} = 0$. The result of irradiation by the VP is a gradual vaporization of the target sheet which we observe using the shadowgraphy imaging system as discussed further in Sec. III B.

III. RESULTS AND DISCUSSION

A. Target selection

To determine the moments at which the sheet reaches $R^{\star}$ for the chosen PP energies of $E_{\mathrm{PP}} = 12\,\mathrm{mJ}$ and 20 mJ, we first investigate the sheet size evolution $R_{\mathrm{sheet}}(t)$ presented in Fig. 1(b). After PP impact, the sheet expands with an initial rate $\dot{R}_0$. With a higher PP energy, $\dot{R}_0$ is larger, and hence less time is required to reach $R^{\star}$. For the case of $E_{\mathrm{PP}} = 20\,\mathrm{mJ}$, the sheet attains this specific size at $t = 1.2\,\mu\mathrm{s}$. We refer to this target as target A. For the lower energy case of $E_{\mathrm{PP}} = 12\,\mathrm{mJ}$, $R^{\star}$ is first reached at $t = 2.1\,\mu\mathrm{s}$. We refer to

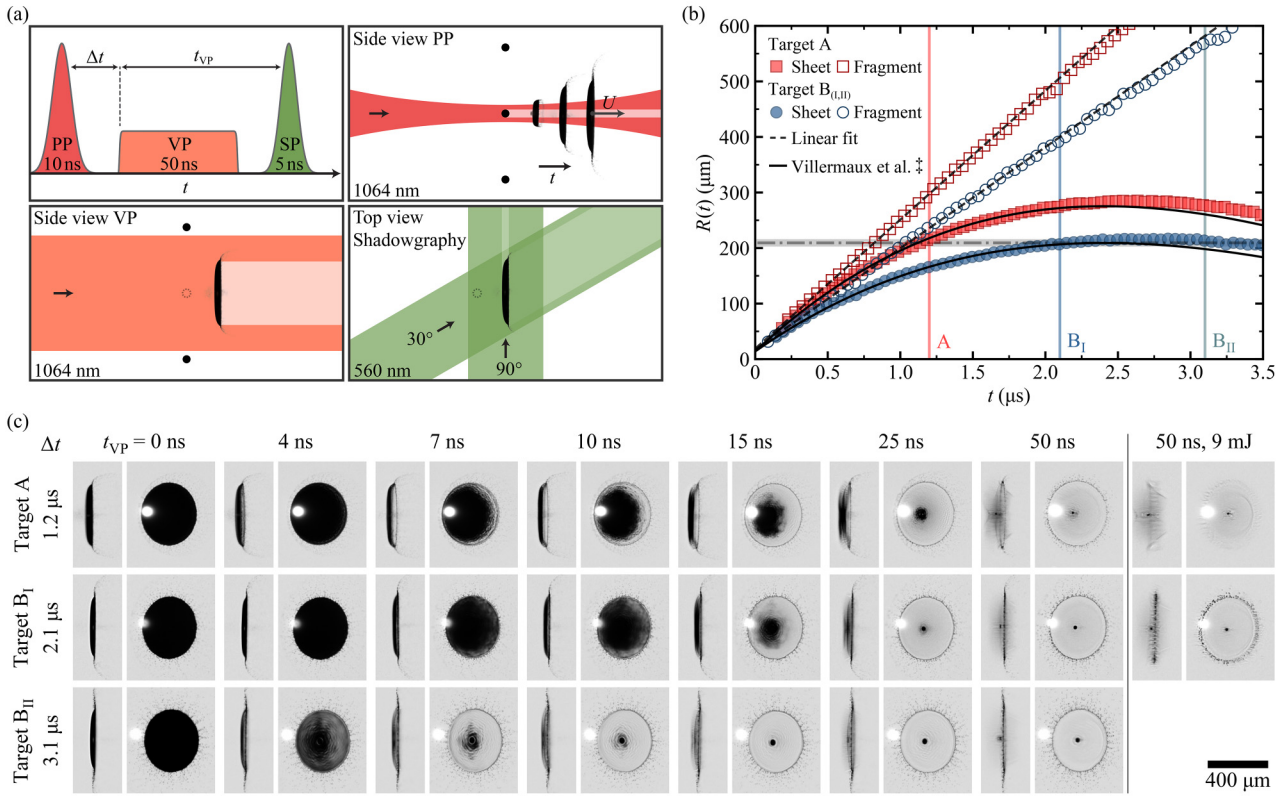

FIG. 1. (a) Illustration of the laser pulse sequence and the respective irradiation geometries. Upper-left: timing of the irradiation scheme, starting with the pre-pulse (PP), followed by the vaporization pulse (VP) after a time interval Δt. To visualize the dynamics of the tin target, the shadowgraphy illumination pulse (SP) is scanned through time t, where $t = 0$ marks the onset of the PP. The start of the VP is indicated by time delay $t_{VP} = 0$. Upper-right and lower-left: side-view schematics of the irradiation conditions during PP and VP, respectively. Lower-right: top-view of 30° and 90° shadowgraphy backlighting. (b) Sheet expansion radius R_{sheet} and farthest fragments distance-to-center $R_{fragment}$ as a function of time t for two PP energies (20 mJ and 12 mJ). The horizontal dash-dotted line (along with a shaded area to indicate the uncertainty) is at a constant 210 μm radius (i.e., $R^\star$). This line intersects the R_{sheet} curves at t =1.2, 2.1, and 3.1 μs (as indicated by the vertical lines), at which moments the sheets are referred to as targets A, B_I, and B_{II}, respectively. The solid lines (‡) following R_{sheet} are fits of the model from Ref. 14 to the data up to 2 μs. The dashed lines along $R_{fragment}$ result from a linear fit to the data up to 1.5 μs. (c) Series of side-view (left) and front-view (right) shadowgraphy images of the three targets during illumination by the VP for different time delays. The VP energy $E_{VP} = 5$ mJ excluding the last column, where $E_{VP} = 9$ mJ. At $t_{VP} = 0$, all three targets share a common sheet size $R^\star$ (i.e., $R_{sheet} \approx 210\,\mu$m).

this target as target B_I. After passing the apex of its expansion trajectory, the sheet retracts due to the surface tension exerted at the sheet edge[7,10,11] and again acquires $R^\star$ at $t = 3.1\,\mu$s, which we refer to as target B_{II}. We find that $R_{sheet}(t)$ agrees well with the analytical model developed by Villermaux and Bossa[14] for the analogous case of droplet impact onto a pillar. Such an agreement has been previously reported in Ref. 10. By fitting this model to the data, we obtain the initial expansion rate $\dot{R}_0$ (for $E_{PP} = 20$ and 12 mJ, $\dot{R}_0 = 244$ and 182 m/s, respectively) with it being the only free fit parameter. Figure 1(b) also presents the radial position of the furthest fragments as a function of time $R_{fragment}(t)$. We find that these fragments follow an expected ballistic trajectory,[23] the slope of which matches the initial expansion rate of the sheet $\dot{R}_0$. We note the significant difference in the distance between the outermost fragments and the sheet edge for the three targets. Each of these three targets, with the common sheet size of $R^\star$, is irradiated by the VP to infer the thickness profile $h(r)$ and mass content of the sheet.

B. Target vaporization

Figure 1(c) presents the front- and side-view shadowgraphy images of the targets through the duration of the VP with an energy of $E_{VP} = 5$ mJ. At the beginning of the VP (i.e., $t_{VP} = 0$), the images show that the main features of these targets include a sheet of liquid tin that is surrounded by small fragments. During VP illumination, we observe a gradual mass removal from the sheet as it becomes transparent to the background illumination light. The vaporized material does not significantly impede the shorter-wavelength shadowgraphy light and, thus, is not expected to

influence the vaporization pulse. Over time, this transparency is seen to move from the periphery inward toward the center of the sheet, leaving a retreating inner sheet with a radius R_{inner}. Given the fact that the VP has a uniform intensity across the beam profile, we reasonably assume that more time is needed to vaporize a sheet that contains more tin and, as a result of the common sheet-size $R^{\star}$, is also thicker. Among the three targets, target A requires the longest time for its sheet to be completely vaporized, followed by targets B_I and B_{II}. We infer that the respective global sheet thicknesses and volumes follow the same order. As a side note, we find that the periphery of target A starts to show transmission prior to that of target B_I ($t_{VP} = 7$ ns). When the periphery of the sheet is removed, a bounding rim appears (see, e.g., front-view images at $t_{VP} = 25$ ns). Such a bounding rim has been widely reported in various scenarios of droplet impact on a solid.[14,16,17,24–26] For the case of laser–droplet impact, the thickness and mass of this rim has been analytically estimated in our previous work[11] and now is visualized. Note that for target B_{II}, the sheet as a whole appears to become transparent almost simultaneously [see Fig. 1(c) at $t_{VP} = 4$ ns] instead of gradually retreating inward. This is due to the vaporization taking place on a timescale similar to the duration (≈ 5 ns) of the shadowgraphy illumination pulse.

By the end of the VP ($t_{VP} = 50$ ns), the sheet is completely removed for all targets. In contrast, the rim and many of the fragments are still present, indicating that the sheet is much thinner than the rim and fragments, as was also identified in Ref. 11. Although the rim and most of the fragments are not fully resolved by our imaging system, from the observed contrast[27] we do infer that target A has a thinner rim (with a diameter of approximately 1–2 μm) and finer fragments compared to the other targets. In fact, target A has such small-sized fragments that a VP of 5 mJ is capable of vaporizing a significant fraction of them by the end of the VP. With a higher VP energy of 9 mJ, all the fragments and the rim of target A are completely vaporized [see the rightmost column in Fig. 1(c)]. In contrast, for targets B_I and B_{II}, no clear vaporization of fragments is observed for a 5 mJ VP, and even with the 9 mJ VP some fragments and leftovers of the rim remain for target B_I. Besides the rim and fragments, a remnant of tin resides at the center of the sheet ($t_{VP} = 50$ ns). Its presence after VP irradiation indicates that also its thickness is significantly larger than that of the sheet. The existence of this center mass is also consistent with our previous observations in Ref. 11.

In Fig. 2(a), we present the radius of the inner sheet $R_{inner}(t_{VP})$ as it evolves throughout the VP duration. The inner radii have been retrieved from shadowgraphy images such as those shown in Fig. 1(c). Again, in Fig. 2(a), we identify that R_{inner} reduces over time for all targets, among which that of targets A and B_{II} decreases at the slowest and the fastest rate, respectively. In the experiment, we found that at a given location r on the sheet, the local time $\tilde{t}_{VP}(r)$ required for the VP to vaporize the local thickness $h(r)$ is inversely proportional to I_{VP}. This has been systematically observed in a scan for various VP pulse energies (ranging from 2 to 9 mJ). The linear proportionality $\tilde{t}_{VP}(r) \propto I_{VP}^{-1}$ indicates that the thickness $h(r)$ is proportional to the VP energy locally deposited in the sheet, i.e., $h(r) \propto I_{VP}\tilde{t}_{VP}(r)$. With a constant VP intensity I_{VP},

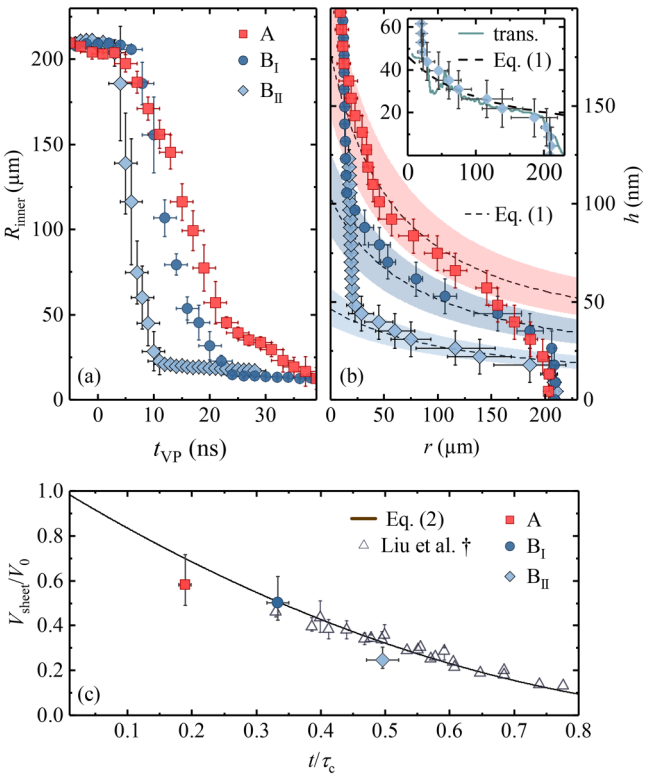

FIG. 2. (a) Radius of the inner sheet R_{inner} as a function of t_{VP} during VP-induced vaporization. (b) Sheet thickness h, obtained by $h(r) = \tilde{t}_{VP}(r)\dot{h}$, as a function of radial position r. The time-averaged vaporization rate $\dot{h}$ is obtained by fitting the thickness of target B_{II} obtained from the transmission method to the corresponding data of $t_{VP}(R_{inner})$, see the main text. The result of this fit is presented in the inset. The thickness model given in Eq. (1) is presented by the dashed line, with the shaded region indicating the uncertainty propagated from $R_0 \pm 0.5\,\mu$m and $\dot{R}_0 \pm 5\%$. (c) Volume ratio of the sheet to the initial droplet V_{sheet}/V_0 as a function of the scaled time t/τ_c, where $\tau_c = 6.6\,\mu$s, with values $0.58^{+0.13}_{-0.09}$, $0.50^{+0.12}_{-0.08}$, and $0.25^{+0.06}_{-0.04}$ for targets A, B_I, and B_{II}, respectively. Previously reported data (open triangles) from Ref. 11 (†) are presented alongside the new results. The solid line depicts Eq. (2).

we can thus conclude $h(r) = \tilde{t}_{VP}(r)\dot{h} \sim \tilde{t}_{VP}(r)$, where $\dot{h}$ refers to a time-average vaporization rate. We make the ansatz that $\dot{h}$ is independent of the local thickness. Thus, the thickness profile of the sheet can be directly obtained from inner radii shown in Fig. 2(a) by exchanging the x- and y-axes and using a single overall scaling factor $\dot{h}$.

C. Thickness and mass content of the targets

In Ref. 11, a partial transparency of the sheet to the shadowgraphy backlighting was used to determine the sheet thickness profile. A significant transmission signal can only be obtained if the sheet is sufficiently thin. We find that this transmission method can be applied to the thinnest target, B_{II}, and we determine its sheet thickness before VP impact ($t_{VP} = 0$). Subsequently, we are able to

determine the scaling factor $\dot{h}$ from a fit such that $h(r) = \tilde{t}_{VP}(r)\dot{h}$ for target B_{II} matches its thickness as acquired from the transmission method in absolute terms, as presented in the inset of Fig. 2(b). The fit shows excellent agreement between the two methods regarding the shape of the sheet thickness. This fit yields $\dot{h} = 4.4(4)\,\mathrm{m/s}$, with the systematic uncertainty in brackets originating from uncertainties in the background correction related to, e.g., dark noise or plasma glare.[11,27] The obtained $\dot{h}$ lies in the range of values obtained in other studies of the ablation of metals under similar irradiation conditions (here the VP fluence is $\approx 0.7\,\mathrm{J/cm^2}$).[28,29] With the known value of $\dot{h}$, we are able to plot the thickness profiles for targets A and B_I.

Figure 2(b) presents the sheet thickness $h(r) = \tilde{t}_{VP}(r)\dot{h}$ as a function of the radial position r for all targets. Moreover, we plot the semi-empirical thickness model[11]

$$h(r,t) = \frac{D_0^3}{1.65\,(\dot{R}_0\,t)^2 + 6.9\,t\,r\dot{R}_0 - 2.4\,r^2}. \tag{1}$$

It is shown in Fig. 2(b) and its inset that Eq. (1) agrees well with the current thickness profiles, both obtained from $h(r) = \tilde{t}_{VP}(r)\dot{h}$ and, for target B_{II}, also from the independent measurement from the transmission method. Here, we employ the initial expansion rate $\dot{R}_0$ as the characteristic velocity in Eq. (1) instead of the center-of-mass speed U as originally used in Ref. 11. This substitution is motivated by a relatively strong deviation from the $\dot{R}_0 \sim U$ similarity[14,16] for targets B_I, B_{II}, arising from the tight focusing condition of the PP used here. As elucidated in Ref. 7, the spatial distribution of the pressure field exerted by the expanding plasma on the droplet surface influences the ratio $\dot{R}_0/U$. A loosely focused beam (i.e., 105 μm at FWHM in Ref. 11) and also an increasing PP energy[10] effectively results in a spreading pressure distribution that yields $\dot{R}_0/U \approx 1$. In contrast, an increasingly focused pressure field, which, for example, can be achieved by employing a tightly focused beam (i.e., 55 μm at FWHM for the present study), results in a larger fraction of the kinetic energy partitioned to expand the droplet rather than to propel it, and thus $\dot{R}_0/U > 1$. Our analysis indeed shows $\dot{R}_0/U = 1.26$ for targets B_I and B_{II}, and $\dot{R}_0/U = 1.09$ for target A, justifying choosing $\dot{R}_0$ as the relevant velocity describing the deformation dynamics.

The thickness data $h(r)$ shown in Fig. 2(b) enable the determination of the sheet volume by integrating $2\pi r h(r)\delta r$ along the radial coordinate, starting from R_0 to the edge of the sheet.[11,14] The region $r < R_0$ is thus excluded from the integration (cf. Refs. 11 and 14) and with it the center mass remnant [see Fig. 1(c)] that has a different physical origin.[11] Figure 2(c) presents the obtained volume ratio of the sheet to the initial droplet V_{sheet}/V_0 as a function of the non-dimensional time t/τ_c, with capillary time $\tau_c = \sqrt{\rho R_0^3/\sigma} = 6.6\,\mu$s. The data indicate a monotonic decrease of the fraction of tin contained in the sheet over time. At the moment of $t/\tau_c = 0.19$ (i.e., target A), the sheet carries close to 60% of the initial amount of tin. For comparison, the data of V_{sheet}/V_0 from Ref. 11 are also shown in panel (c). Despite the differences in the experimental conditions (regarding R_0, E_{PP}, and the focal spot size of the beam) between the present study and Ref. 11, these two data sets agree well with each other. Additionally, in panel (c) we plot the model

$$\frac{V_{sheet}}{V_0} = \left(1 - \frac{\sqrt{3}}{2}\frac{t}{\tau_c}\right)^2, \tag{2}$$

which was derived in Ref. 11 using the analytical expression of the thickness profile and the radius of the sheet from Ref. 14. Equation (2) was found in Ref. 11 to be able to describe the sheet volume for the laser–droplet impact case. Figure 2(c) shows that in the present study, Eq. (2) is consistent with the experimental findings also in the early time regime. Further experimental data would benefit the detailed study of the full evolution of the sheet thickness and its volume and is needed to attest to the general validity of Eq. (2), in particular, at the early times that have now become accessible employing the laser-induced vaporization method. In short, our results show a good agreement with the prediction from Eq. (2) and match well with our previous study in Ref. 11 in the late-time overlap region. We thus unambiguously demonstrate that increasing the energy of the laser pre-pulse that, crucially, enables the sheet to reach a specified target size more quickly results in a significantly larger mass fraction contained in the sheet.

IV. CONCLUSION

In this paper, we experimentally investigated the mass content of expanding sheets of liquid tin, formed upon nanosecond pre-pulse laser impact on tin microdroplets. An auxiliary vaporization laser pulse was used to gradually remove mass from the liquid sheet, thereby exposing the sheet's thickness profile and mass content. Furthermore, the removal of the sheet revealed and confirmed the presence of a sheet bounding rim and center mass. Three targets, generated by using two different PP energies, were selected at different times during their expansion trajectories such that they all shared a common sheet size $R^\star = 210\,\mu$m. The thickness of the thinnest target has been independently determined by an optical method that has been validated in Ref. 11. The resulting thickness enabled the conversion of the local time of vaporization of the other two targets by the auxiliary pulse to the thickness profiles of the sheets. We have further shown that the thickness for each target agrees well with the model developed in Ref. 11. The spatial integration of the obtained thickness profile yielded the volume fraction of the sheet for each target, for which we found a good agreement with previously reported models. The results confirmed how using a more energetic PP is a favorable strategy for achieving a specified sheet size while minimizing mass loss from the sheet to the bounding rim and fragments. For the target with the highest PP energy studied here, we found that approximately 60% of the mass was still present in the sheet, more than doubling the mass fraction that may be expected to be contained in targets reported in the available literature relevant for the nanolithography industry.[18,19] From the perspective of debris mitigation, such a target may also be preferred as, complementary to a larger sheet mass fraction, less mass is carried by the fragments. Investigations of the thickness profile and target mass at even earlier times after laser pulse impact are accessible by the laser-vaporization method. Our findings and method can serve a crucial role in the optimization of PP parameters, maximizing the tin mass available for the

production of EUV light in tin-droplet-based plasma sources for nanolithography.

AUTHORS' CONTRIBUTIONS

B.L. and R.A.M. contributed equally to this work.

ACKNOWLEDGMENTS

The authors thank Haining Wang, Wim van der Zande, and Joost Frenken for fruitful discussions. This work has been carried out at the Advanced Research Center for Nanolithography (ARCNL), a public-private partnership of the University of Amsterdam (UvA), the Vrije Universiteit Amsterdam (VU), the Netherlands Organisation for Scientific Research (NWO), and the semiconductor equipment manufacturer ASML. This project has received funding from European Research Council (ERC) Starting Grant number 802648 and is part of the VIDI research programme with Project Number 15697, which is financed by NWO.

DATA AVAILABILITY

The data that support the findings of this study are available from the corresponding author upon reasonable request.

REFERENCES

[1]Y. Tao, M. S. Tillack, K. L. Sequoia, R. A. Burdt, S. Yuspeh, and F. Najmabadi, "Efficient 13.5 nm extreme ultraviolet emission from Sn plasma irradiated by a long CO_2 laser pulse," Appl. Phys. Lett. **92**, 251501 (2008).
[2]J. Benschop, V. Banine, S. Lok, and E. Loopstra, "Extreme ultraviolet lithography: Status and prospects," J. Vac. Sci. Technol. B **26**, 2204–2207 (2008).
[3]S. Fujioka, M. Shimomura, Y. Shimada, S. Maeda, H. Sakaguchi, Y. Nakai, T. Aota, H. Nishimura, N. Ozaki, A. Sunahara, K. Nishihara, N. Miyanaga, Y. Izawa, and K. Mima, "Pure-tin microdroplets irradiated with double laser pulses for efficient and minimum-mass extreme-ultraviolet light source production," Appl. Phys. Lett. **92**, 241502 (2008).
[4]V. Y. Banine, K. N. Koshelev, and G. H. P. M. Swinkels, "Physical processes in EUV sources for microlithography," J. Phys. D **44**, 253001 (2011).
[5]I. Fomenkov, D. Brandt, A. Ershov, A. Schafgans, Y. Tao, G. Vaschenko, S. Rokitski, M. Kats, M. Vargas, M. Purvis, R. Rafac, B. La Fontaine, S. De Dea, A. LaForge, J. Stewart, S. Chang, M. Graham, D. Riggs, T. Taylor, M. Abraham, and D. Brown, "Light sources for high-volume manufacturing EUV lithography: Technology, performance, and power scaling," Adv. Opt. Technol. **6**, 173–186 (2017).
[6]O. O. Versolato, "Physics of laser-driven tin plasma sources of EUV radiation for nanolithography," Plasma Sources Sci. Technol. **28**, 083001 (2019).
[7]H. Gelderblom, H. Lhuissier, A. L. Klein, W. Bouwhuis, D. Lohse, E. Villermaux, and J. H. Snoeijer, "Drop deformation by laser-pulse impact," J. Fluid Mech. **794**, 676–699 (2016).
[8]D. Kurilovich, A. L. Klein, F. Torretti, A. Lassise, R. Hoekstra, W. Ubachs, H. Gelderblom, and O. O. Versolato, "Plasma propulsion of a metallic microdroplet and its deformation upon laser impact," Phys. Rev. Appl. **6**, 014018 (2016).
[9]D. Kurilovich, M. M. Basko, D. A. Kim, F. Torretti, R. Schupp, J. C. Visschers, J. Scheers, R. Hoekstra, W. Ubachs, and O. O. Versolato, "Power-law scaling of plasma pressure on laser-ablated tin microdroplets," Phys. Plasmas **25**, 012709 (2018).
[10]A. L. Klein, D. Kurilovich, H. Lhuissier, O. O. Versolato, D. Lohse, E. Villermaux, and H. Gelderblom, "Drop fragmentation by laser-pulse impact," J. Fluid Mech. **893**, A7 (2020).
[11]B. Liu, D. Kurilovich, H. Gelderblom, and O. O. Versolato, "Mass loss from a stretching semitransparent sheet of liquid tin," Phys. Rev. Appl. **13**, 024035 (2020).
[12]D. Hudgins, N. Gambino, B. Rollinger, and R. Abhari, "Neutral cluster debris dynamics in droplet-based laser-produced plasma sources," J. Phys. D **49**, 185205 (2016).
[13]F. Torretti, J. Sheil, R. Schupp, M. Basko, M. Bayraktar, R. Meijer, S. Witte, W. Ubachs, R. Hoekstra, O. Versolato *et al.*, Prominent radiative contributions from multiply-excited states in laser-produced tin plasma for nanolithography," Nat. Commun. **11**, 1–8 (2020).
[14]E. Villermaux and B. Bossa, "Drop fragmentation on impact," J. Fluid Mech. **668**, 412–435 (2011).
[15]A. L. Klein, W. Bouwhuis, C. W. Visser, H. Lhuissier, C. Sun, J. H. Snoeijer, E. Villermaux, D. Lohse, and H. Gelderblom, "Drop shaping by laser-pulse impact," Phys. Rev. Appl. **3**, 044018 (2015).
[16]Y. Wang and L. Bourouiba, "Drop impact on small surfaces: Thickness and velocity profiles of the expanding sheet in the air," J. Fluid Mech. **814**, 510–534 (2017).
[17]Y. Wang, R. Dandekar, N. Bustos, S. Poulain, and L. Bourouiba, "Universal rim thickness in unsteady sheet fragmentation," Phys. Rev. Lett. **120**, 204503 (2018).
[18]Y. Tao, J. T. Stewart, J. Jur, A. LaForge, D. Brown, M. J. Arcand, A. A. Schafgans, and M. A. Purvis, "Extreme ultraviolet light source," ASML Netherlands B.V., U.S. patent 20160007434A1 (7 January 2016).
[19]M. Purvis, I. V. Fomenkov, A. A. Schafgans, P. Mayer, K. Hummler, M. H. Leenders, Y. Tao, S. I. Rokitski, J. Stewart, A. I. Ershov, R. J. Rafac, S. D. Dea, G. O. Vaschenko, D. C. Brandt, and D. J. Brown, Proc. SPIE **11111**, 111110K (2019).
[20]D. Kurilovich, "Laser-induced dynamics of liquid tin microdroplets," Ph.D. thesis (Vrije Universiteit Amsterdam, 2019).
[21]S. A. Reijers, D. Kurilovich, F. Torretti, H. Gelderblom, and O. O. Versolato, "Laser-to-droplet alignment sensitivity relevant for laser-produced plasma sources of extreme ultraviolet light," J. Appl. Phys. **124**, 013102 (2018).
[22]R. A. Meijer, A. S. Stodolna, K. S. E. Eikema, and S. Witte, "High-energy Nd:YAG laser system with arbitrary sub-nanosecond pulse shaping capability," Opt. Lett. **42**, 2758–2761 (2017).
[23]Y. Wang and L. Bourouiba, "Unsteady sheet fragmentation: Droplet sizes and speeds," J. Fluid Mech. **848**, 946–967 (2018).
[24]A. Rozhkov, B. Prunet-Foch, and M. Vignes-Adler, "Dynamics of a liquid lamella resulting from the impact of a water drop on a small target," Proc. R. Soc. London **460**, 2681–2704 (2004).
[25]J. Eggers, M. Fontelos, C. Josserand, and S. Zaleski, "Drop dynamics after impact on a solid wall: Theory and simulations," Phys. Fluids **22**, 1063 (2010).
[26]H. Lastakowski, F. Boyer, A.-L. Biance, C. Pirat, and C. Ybert, "Bridging local to global dynamics of drop impact onto solid substrates," J. Fluid Mech. **747**, 103–118 (2014).
[27]J. Blaisot and J. Yon, "Droplet size and morphology characterization for dense sprays by image processing: Application to the diesel spray," Exp. Fluids **39**, 977–994 (2005).
[28]M. S. Qaisar and G. J. Pert, "Laser ablation of Mg, Cu, and Pb using infrared and ultraviolet low-fluence lasers," J. Appl. Phys. **94**, 1468–1477 (2003).
[29]C. Porneala and D. A. Willis, "Time-resolved dynamics of nanosecond laser-induced phase explosion," J. Phys. D **42**, 155503 (2009).